 doi:10.20944/preprints202111.0422.v1

Type of the Paper (Article)

Real-time tephra detection and dispersal forecasting by a ground-based weather radar

Magfira Syarifuddin[1,*], Susanna F. Jenkins[2], Ratih Indri Hapsari[3], Qingyuan Yang[4], Benoit Taisne[5], Andika Bayu Aji[6], Nurnaning Aisyah[7], Hanggar Ghanara Mawanda[8], Djoko Legono[9].

[1] Earth Observatory of Singapore, Asian School of the Environment, Nanyang Technological University; magfira.syarifuddin@ntu.edu.sg
[2] Earth Observatory of Singapore, Asian School of the Environment, Nanyang Technological University; susanna.jenkins@ntu.edu.sg
[3] State Polytechnic of Malang; ratih@polinema.ac.id
[4] Earth Observatory of Singapore, Asian School of the Environment, Nanyang Technological University; qingyuan.yang@ntu.edu.sg
[5] Earth Observatory of Singapore, Asian School of the Environment, Nanyang Technological University; BTaisne@ntu.edu.sg
[6] Earth Observatory of Singapore, Asian School of the Environment, Nanyang Technological University; ANDIKABA001@e.ntu.edu.sg
[7] Centre for Volcanology and Geological Hazards Mitigation; aisyahnaning@gmail.com
[8] Gadjah Mada University; hanggarmawandha@gmail.com
[9] Gadjah Mada University; djokolegono@yahoo.com

* Correspondence: magfira.syarifuddin@ntu.edu.sg

Abstract: Tephra plumes can cause a significant hazard for surrounding towns, infrastructure, and air traffic. The current work presents the use of a small and compact X-band Multi-Parameter (X-MP) radar for the remote tephra detection and tracking of two eruptive events at Merapi Volcano, Indonesia, in May and June 2018. Tephra detection was done by analysing the multiple parameters of radar: copolar correlation and reflectivity intensity. These parameters were used to cancel unwanted clutter and retrieve tephra properties, which are grain size and concentration. Real-time spatial and temporal forecasting of tephra dispersal was performed by applying an advection scheme (nowcasting) in the manner of Ensemble Prediction System (EPS). Cross-validation was done using field-survey data, radar observations, and Himawari-8 imagery. The nowcasting model computed both the displacement and growth and decaying rate of the plume based on the temporal changes in two-dimensional movement and tephra concentration, respectively. Our results with ground-based data, where the radar-based estimated grain size distribution fell within the range of *in-situ* data. The uncertainty of real-time forecasted tephra plume depends on the initial condition, which affects the growth-and decaying rate estimation. The EPS improves the predictability rate by reducing the number of missed and false forecasted events. Our findings and the method presented here are suitable for early warning of tephra fall hazard at the local scale.

Keywords: tephra; ground-based weather radar; Bayesian approach; nowcasting; ensemble prediction system.

1. Introduction

Tephra is the fragmented material produced during an explosive volcanic eruption. Once in the atmosphere, the mix of tephra, volcanic gases, and ambient air forms a volcanic plume. Tephra is classified according to its size as volcanic bombs or blocks ($D \geq 64$ mm or $\phi \leq -6$), lapilli (2 mm $\leq D < 64$ mm or $-1 \geq \phi > -6$), coarse ash (64 μm $\leq D < 2$ mm or $4 \geq \phi > -1$), and fine ash ($D < 64$ μm or $\phi > 4$), where D is the diameter of the particle and $\phi \equiv -\log 2D$ (mm). Tephra falls can damage buildings and cause disruption to human livelihoods, agricultural production, and other economic activities [1-3]. Because of the

significance of the hazards posed by tephra fall, its timely detection and tracking in the atmosphere is very important.

Tephra can be detected and tracked in the atmosphere with ground-based weather radars operating at various wavelengths [4-7]. Tephra properties (concentration, fall rate, and diameter) have been retrieved by radar using a microphysical model of atmospheric scattering theorem, which assumed that tephra particles have similar characteristics to raindrops [8-11]. One of the radar applications that has not been explored thoroughly is its use as an extension to an early-warning system of spatial and temporal tephra dispersal. Up to now, only one study has documented the use of weather radar for early-onset detection and tracking of tephra [6]. In this previous study, the detection of plume onset was achieved by coupling radar and an infrasound instrument. However, tracking of the plume excluded the sources and sink of radar observable [6]. As a result, the tephra plume's spatial movement (displacement) was monitored, but the observable radar values were constant through time, indicating a persistent presence of volcanic clouds in the atmosphere. A solution for this problem is applying a dynamic advection scheme, widely used for atmospheric precipitation forecasting [6], known as nowcasting [12-15]. Nowcasting is a spatial prediction method covering minutes to a few hours of rainfall forecasting based on radar advection vectors. This approach can forecast the rotation and deformation of the observed field and has been an essential prerequisite for real-time flash flood forecasting in operational hydrology [13].

Recently, ensemble prediction system (EPS) has attracted the interest of modellers, as it can increase the robustness of forecasting results [14-16]. When applying the EPS, the nowcasting model is run multiple times from very slightly different initial conditions. This approach has been applied to the volcanic ash retrieval model to increase the predictability score of volcanic cloud dispersal forecasting for the 2014 Kelud and 2015 Rinjani eruptions [17]. Their study found that poorer prediction skills could result from using shorter time steps and incorrect threshold of volcanic ash mass load. The later mentioned reason is related to the limitation of satellite monitoring, particularly at lower altitudes and in surrounding and overlying cloud features not involving ash, which could also account for the discrepancies in the low mass load regions. Moreover, the satellite based-volcanic ash retrieval model requires atmospheric condition data and eruptive source parameters (ESP), i.e., plume height, grain size distribution (GSD), and wind field. Those requirements can complicate the calculation process as they are often unknown until after the eruption. Contrarily, a weather radar provides atmospheric information near ground surface level (< 3000 m height) and can directly estimate the GSD and concentration of tephra [8-11; 18-19], which can then be used as robust ESP for a radar nowcast model.

This study presents the potency and uncertainty of real-time tephra plume detection and tracking applied to two eruption events at Merapi in 2018. First, we overcome previous limitations of unwanted clutter contaminating radar scanning data [19] by applying an automatic noise cancellation. Then, we coupled the modified tephra-radar retrieved model [8-9,18-19] with the EPS of radar nowcasting. The evaluation was done by comparing the radar-based tephra properties (i.e., concentration and grain size) with ground-based data and satellite imagery. Through this study, the integration of EPS forecast products can contribute to the potential use of weather radar monitoring in the tephra fall early warning system, which is beneficial for local people living nearby Merapi.

2. Methods

2.1 Radar Setting and study case

A small-compact X-band dual-polarization Doppler weather Multi-Parameter (X-MP) of WR2100 type radar, manufactured by Furuno Electric Co, was installed and operated at Merapi Museum (7.5 km SW from Merapi's vent) in 2014-2019 (Figure 1). The main objective of the installation was for research in volcano hazards such as rain-triggered lahar [16, 20] and real-time tephra fallout rate [19]. Figure 1 presents the area covered by the 360° radar scan of plan position indicator (PPI) strategy. In PPI scanning mode, the

Preprints (www.preprints.org) | NOT PEER-REVIEWED | Posted: 23 November 2021 doi:10.20944/preprints202111.0422.v1

radar scans the volume of the atmosphere by changing the elevation angle in sequence every time it finishes one rotational scan. There were nine different elevation angles: 3, 5, 7, 9, 11, 13, 15, 18, and 21°. An entire volumetric scan sampled the atmosphere into 700 sweeps (beam motion), and each sweep had 300 range gates with 150 m bin width. It requires 2 min time intervals for a full volumetric PPI scan (all elevation angles). Radar data were heavily affected by ground clutter up to 13° elevation angle scan (Figure 1). While the default clutter cancellation routine by radar can recognize the beam blockage [20], ground clutter still occurred as the result of direct contact between surface and sidelobes due to the presence of Merapi and Turgo Hill in the SW sector (Figure 1, [19]). Sidelobes are unwanted returns from a direction outside the main lobe, which can bias the reflectivity intensity, Doppler velocity, and spectrum width estimates.

Table 1 presents the specification of this small, compact, and light-weighted system. This ground-based weather radar is a dual-polarized system that transmits two different wavelength propagations: horizontal and vertical, giving multiple output parameters, listed in Table 1. Only two parameters were used in this study: the reflectivity intensity Z_H and copolar correlation ρ. Reflectivity intensity in horizontal copolar propagation Z_H measures the efficiency of a target to reflect (absorb and re-radiate) radar energy. The copolar correlation ρ, is the zero-lag correlation coefficient between horizontally (H) and vertically (V) transmitted and received copolar signals. This parameter shows the uniformity of the features being observed by the radar. Detailed explanations for each of the dual-polarized system's radar parameters have been discussed in [21]. Both Z_H and ρ were used to remove unwanted clutter, and only the filtered Z_H was used for tephra detection and tracking, explained in **sections 2.2-2.3** and **Appendix A**.

The selected study cases are two explosive events with the availability of X-MP radar data and in-situ tephra grain size information [23], on May 11, 2018 (M05) and June 01, 2018 (M06). Following Merapi's last centennial explosive eruption in 2010, the volcano experienced six phreatic eruptions between 2012 and 2014. The M05 event was the first minor explosion after four years of quiescence, starting in 2014. It occurred at 0040 (time is expressed in *hhmm* UTC) and lasted for 5-mins. The Centre for Research and Technology of Geological Disasters (*Balai Penyelidikan dan Pengembangan Teknologi Kebencanaan Geologi – BPPTKG*) officially reported it as a phreatic eruption. Prior to the eruption, there were no unequivocal precursory signals, which is common for this type of eruption. The event produced a 5.5 km high (above its summit) eruption column with explosion energy of 17 MJ [24].

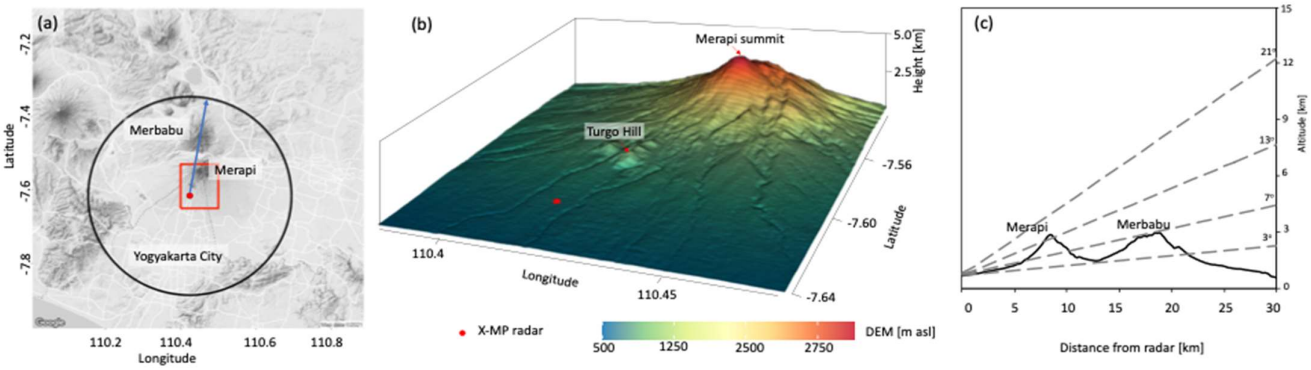

Figure 1. Left panel (a) is a fixed observation area of the PPI scan mode. Centre panel (b) is the 3-D view of surface topography of the red square area in (a). Right panel (c) is the vertical profile of radar scan and topography, extracted along the blue arrow in (a). Identified are location of Yogyakarta city, Merapi summit, Merbabu, Turgo hill, and the location of X-MP radar, indicated by a red dot in (a) and (b).

Preprints (www.preprints.org) | NOT PEER-REVIEWED | Posted: 23 November 2021 doi:10.20944/preprints202111.0422.v1

Table 1. Radar specification used in the study [22]

Parameter	Description
Transmitter	Solid-state 200 W per channel (H, V)
Polarity	Dual polarimetric horizontal (H) and vertical (V)
Pulses	PRF 600-2500 Hz, Width 0.1-5.0 μs
Antenna	0.75 m ∅, 2.7° beam width
Antenna gain	33.0 dBi
Operating Frequency	9.47 GHz
Wavelength	3.3 cm
Peak Power	100 W
Scan mode	PPI, CAPPI, RHI
Maximum distance display	50 km
Maximum range fixed observation level	30 km
Data output	1) Reflectivity Intensity – Z_H [dBZ], 2) Doppler velocity – V_D [m s^{-1}], 3) Doppler velocity spectrum width - W_D [m s^{-1}] 4) Differential reflectivity –Z_{DR} [dB], 5) Specific differential phase shift – K_{DP} [°km^{-1}] 6) Copolar correlation coefficient - ρ 7) Rainfall intensity – R [mm h^{-1}], 8) Cross polarization difference phase - ΦDP

Merapi continued its eruptive activity between May 21–24, 2018, by producing multiple explosions. This series of short-lived eruptions ended on June 1, 2018, marked by three explosions that occurred on the same day. The M06 event was the first eruption on that day and had the greatest intensity of the three, occurring at 0120 UTC for a 2-mins duration [25]. The eruption produced a 6 km high eruption column with explosion energy of 46 MJ [24]. Subsequently, Merapi's activities shifted to be more magmatic, marked by the appearance of a new lava dome in August 2018.

Another reason for selecting these explosive events was the different spatial distributions of the pyroclastic deposit. The deposit of tephra fall from M05 was found in the S sector, while M06 deposits were deposited in the NW sector from Merapi [23]. While being small in magnitude (Volcanic eruptive index, VEI-1), satellite images captured both cases (**Appendix C: Figure C.1**), meaning that the reliability of EPS results could be evaluated.

We used a set of radar data of 56-mins, ranging from 4-mins before to 52-mins after the onset. Hence, it gave a range of time scans at 0036-0130 (M05) and 0116-0120 (M06). This time range selection was based on visual verification of tephra visibility on radar images. We also found that the plume was only detected at 13-21o elevation angles.

2.2 Tephra detection

The detection of the volcanic cloud was done by identifying radar echoes of the tephra from non-tephra echoes. Although both cases occurred during clear days, non-tephra noises still occurred because of sidelobe contamination, anomalous propagation, and the presence of ground clutter. Anomalous propagation results from false radar echoes during calm, stable atmospheric conditions, often associated with super refraction in a temperature inversion, which directs the radar beam toward the ground. We applied a clutter cancellation procedure based on Naïve Bayesian Classifier to solve the previously mentioned problems [26].

The Naïve Bayesian Classifier (NBC) is a supervised technique, which implements the classification based on the posterior probability that certain observed measurements correspond to a specific class. In the clutter cancellation process, the unwanted clutters were divided into three classes: the non-clutter data (c=0), clutter (c=1), and invalid data (c=-99). The third class was introduced based on the radar signal/beam blocking identified

Preprints (www.preprints.org) | NOT PEER-REVIEWED | Posted: 23 November 2021 doi:10.20944/preprints202111.0422.v1

by the Furuno default rain-map program [20]. For our study, only data corresponding to the non-clutter class was recognized as valid and used for tephra detection and tracking.

The 2-D spatial data of reflectivity intensity Z_H was used as the input parameter in the volcanic ash retrieval radar model (VARR, [8-9]). This method is a two-step stepwise approach radar microphysical model, using the scaled gamma distribution. The scattering of electromagnetic waves from tephra particles follows the Rayleigh theorem [8-9]. Only coarse ash to lapilli regimes were identified by this type of radar [18-19], resulting in two different tephra class regimes: fine (F) and coarse (C) particle. These two terms should be distinguished from finer ash and coarser ash regimes, mentioned in section 1, as our classification identified class F as a class for particle diameter ranging from 0.015 mm to 0.35 mm and class C for particle diameter ranging from 0.35 mm to 6 mm. This range was generated based on the previous study [8-9, 18-19]. Table A.1 presents detailed information about tephra classification. The clutter cancellation and radar-tephra retrieved model are discussed intensively in [26] and [8-9, 18], respectively; hence, only a brief description is presented in **Appendix B** for convenience.

2.3 Nowcasting and ensemble prediction system

Tracking of tephra was done by adopting the radar's observable extrapolation model, originally known as the translation model [12]. In meteorology, radar's Constant Altitude PPI (CAPPI) data are widely used to estimate the surface level of rainfall intensity. However, there is no agreement regarding which radar product should be used to estimate tephra properties. Essentially, CAPPI is the 3-Dimensional (3-D) interpolated data of PPI, and some studies have used this type of data to estimate the tephra fallout rate [19,27]. Meanwhile, other studies have used the lowest PPI elevation angle data to estimate the accumulated tephra deposit [28, 29]. In this study, we used the maximum aggregates of radar observable as suggested in [30]. The maximum reflectivity intensity is usually related to the densest concentration of tephra [29]. For each 2-mins time acquisition of the PPI scan, we calculated the maximum aggregate of tephra concentration across all elevation angle 13-21°. This aggregate value was compiled as gridded 2-D (150 m mesh) spatial data. The use of a maximum aggregate was also used to tackle the problem of wavelength sensitivity, which caused the underestimation of retrieved tephra properties [19, 31]. Using the radar parameter, i.e., reflectivity intensity factor Z_H, to estimate tephra concentration, we could simplify the forecast of tephra dispersion, as this approach did not require the atmospheric condition and ESP information. In this study, we used the estimated tephra concentration from the tephra detection framework to estimate the dynamic of its distribution along x and y directions and time t as follows

$$\frac{\partial C_a}{\partial t} + m\frac{\partial C_a}{\partial x} + m\frac{\partial C_a}{\partial y} = w \tag{1}$$

where, $m = dx/dt$ and $n = dy/dt$ were radar advection vectors and $w = dC_a/dt$ was the radar echo growth and decaying rate (source/sink term). The spatial coordinate (x,y) represented easting and northing UTM, respectively. Variables m, n, and w were defined in eqs. (2.1-2.3)

$$m(x,y) = c_1x + c_2y + c_3 \tag{2.1}$$

$$n(x,y) = c_4x + c_5y + c_6 \tag{2.2}$$

$$w(x,y) = c_7x + c_8y + c_9 \tag{2.3}$$

Ensemble forecasting or EPS could help to get a feeling for the possibilities of pattern evolution. In eqs. (2.1)–(2.3), $c_1 - c_9$ parameters were optimized by linear least square using past estimated tephra concentration, whereas in this case, the first 4-8 minutes detected plume captured in radar images. Nowcasting could be run according to different phenomena, which led to different ensemble member scenarios (Table 2). Considering the importance of the growth and decay rate to accommodate the sources and sinks of plume presence in the atmosphere, we selected phenomena 4 and 5 in Table 2. For each advection

Preprints (www.preprints.org) | NOT PEER-REVIEWED | Posted: 23 November 2021 doi:10.20944/preprints202111.0422.v1

phenomenon, the ensemble member was modelled by various sets of time-lagged forecasts starting at different initial times [32]. As the first visible plume on radar imageries occurred simultaneously as the eruption onset and considering the importance of past observed radar data in generating the advection scheme, the selected initial condition was then decided at 4, 6, and 8-mins after the reported onset. Thus, each case had six members, and its subsequent times were separated by 2-mins intervals. The nowcasting model was run up to 44-mins after the eruption onset, as it followed the presence of detected plume in observed radar data. The mean ensemble was obtained by calculating the mean of all members, using the time average of spatial data at each point (x,y). All results were projected and visualized in WGS 84 coordinate system by rgdal and ggmap libraries of RStudio [33,34].

Table 2. Combinations of advection vectors parameter, adopted from different rainfall phenomena [15]

No	Phenomena	c_1	c_2	c_3	c_4	c_5	c_6	c_7	c_8	c_9
1	Parallel translation			X			X			
2	Parallel translation and rotation	X	X	X	X	X	X			
3	Rotation	X	X		X	X				
4	Parallel translation, growth-decay			X			X	X	X	X
5	Parallel translation, rotation, growth-decay	X	X	X	X	X	X	X	X	X

2.4 Evaluation

The reliability of a predictive approach that considers uncertainty was examined, visually and quantitatively, through the verification of those members and observation from radar and Himawari-8. The observed concentration was derived from the valid Z_H data, i.e., the filtered data after removing unwanted clutter. Himawari-8 is a satellite operated by Japan Meteorological Agency (JMA) since 2014, which observes the earth from 80°E to 160°W and between 60°N and 60°S. The Advanced Himawari Imager (AHI) is an optical radiometer onboard the Himawari-8. Its full-disk observation covers 16 spectral bands from visible to infrared (IR) wavelengths. The spatial and temporal resolutions are 2 km and 10-mins, respectively [35]. We assumed this setting caused the Himawari-8 data to be at least 10-mins behind radar data or real-time. The standard Himawari-8 data were retrieved from the P-Tree system, managed by the Japan Aerospace Exploration Agency (JAXA) Earth Observation Research Centre (EORC) and JMA. This study used the temperature band difference of band 13 (BTDB13) as the red beam of $BTD_{B13\text{-}B15}$ was found to be effective for detecting dust and volcanic ash [36]. The identified tephra plume was defined by lower than 285 K cloud temperature above the coordinates of Merapi, which is the temperature at 3-5 km asl height. The 2-D gridded data of Himawari-8 was then transformed into a polygon to delineate the fraction of cloud identified as tephra plume.

Two widely used dichotomous indices were applied: the critical success index (*CSI*) and the probability of detection (*POD*). They were given by the following formulas (eqs. 3-4), along with a confusion matrix presented in Table 3. Here, N_{hit} is the number of hit events from the contingency table, N_{miss} is the number of miss events, and N_{false} is the number of false events as defined in Table 2. The values of these indices have the range 0–1, where "1" represents a perfect forecast.

$$CSI = \frac{N_{hit}}{N_{hit} + N_{miss} + N_{false}} \tag{3}$$

$$POD = \frac{N_{hit}}{N_{hit} + N_{miss}} \tag{4}$$

Preprints (www.preprints.org) | NOT PEER-REVIEWED | Posted: 23 November 2021 doi:10.20944/preprints202111.0422.v1

Table 3. The 2 x 2 confusion matrix [37]

2 × 2 Confusion Matrix		Event Observed	
		YES	NO
Event Forecast	YES	Hit	Miss
	NO	False	Hit

Regarding probabilistic prediction, to date, the most common metric for assessing accuracy is the Brier score [38]:

$$BS = \frac{1}{n}\sum_{k=1}^{n}(y_k - o_k)^2 \quad (5)$$

where y is the fraction of members that forecast the event, o is the actual outcome of the event ("1" if it occurs and "0" if it does not occur), and n is the number of forecasting pairs that are spatial. The score of a perfect forecast was "0". This index was applied to assess probabilistic tephra concentration nowcasting that was equal or greater than 0.01 g/m³.

3. Results

3.1. Volcanic ash detection

Figure 2 shows the results of the Bayesian classifier for tephra detection on M05 and M06 at 2-mins after the onset. All used reflectivity intensity data were cleaned from unwanted clutter by NBC, given by some examples presented in Figure A.1. The spatial and temporal evolution of estimated tephra particles at selected time stamps are given in Figures C.2 and C.3. For both M05 and M06, plumes were identified from 0-min after reported onset up to more than 40-mins and 20-mins after onset, respectively. All particle size classes (ash and lapilli) were identified at the onset of the eruption.

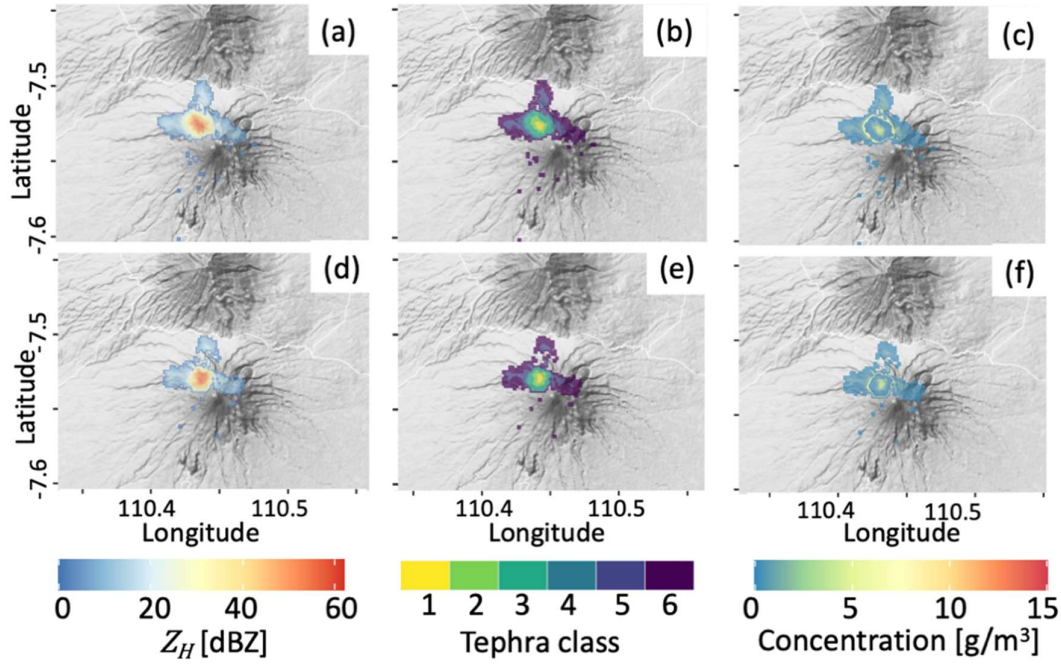

Figure 2. Tephra detection using modified VARR model (**Appendix A** and **B**) for M05 (first row) and M06 (bottom row) at 2-mins after the reported eruption onset. From the left, first column (a and d) is reflectivity intensity, second column (d and e) is tephra classes, and third column (c and f) is tephra concentration. Tephra classes (d and e) of 1-3 represent coarse class (C) of light, moderate, and intense concentration, respectively. Tephra classes of 4-6 represents the same tephra concentration, but for finer class (F).

Preprints (www.preprints.org) | NOT PEER-REVIEWED | Posted: 23 November 2021 doi:10.20944/preprints202111.0422.v1

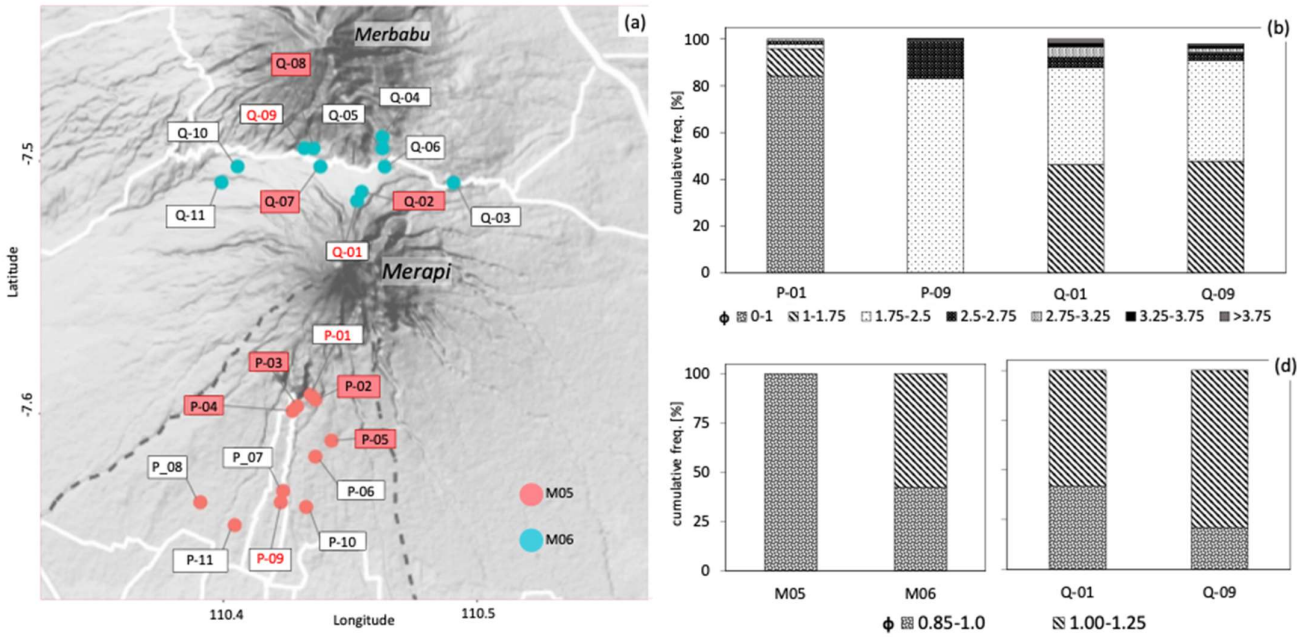

Figure 3. Left panel (a) is the location of *in-situ* sampling points of grain size (ϕ) for both event cases, digitized from [23]. Available data in [23] are Q-01, Q-09, P-01, and P-09 as presented in the cumulative frequency of GSD in (b), where M05 is given by P-01 and P-09, and M06 is given by Q-01 and Q-09 (M06). The cumulative frequency of GSD in (c) is extracted from radar retrieved model for M05: P-01, P-02, P-03, P-04, and P-05; and M06: Q-01, Q-02, Q-07, Q-08, Q-09. The frequency cumulative GSD in (d) is extracted from radar retrieved GSD for Q-01 and Q-09 (M06).

Grain size distributions (in ϕ) of the tephra deposits at sample sites near the volcano [23] and the extracted from the radar retrieved model are presented in Figure 3. Notice that the in-situ sampling points in Figure 3(a) were ground-based data, while radar data represents the elevation angles 13-21° scans. Hence, some *in-situ* data points [23] did not align with temporal radar images. For M05, the *in-situ* data points in [23] were available at P-01 and P-09. Unfortunately, the nowcasting results for this case did not produce any data from these two points. The retrieved concentration was probably eliminated following the unwanted clutter removal (Figure 3c-d). However, we could retrieve GSD from P-02 to P-05 and aggregate their values to represent the GSD for M05. Using nowcasting radar images, we could retrieve tephra concentration and GSD at P02 to P05. P-02 to P-04 were located close to P-01, and P-05 was located a few km distant from P-01. The aggregated GSD could help give the characteristic of M05 GSD. Figure 3 concluded that detected tephra radar retrieved of M05 produced coarser particle distribution than M06.

3.2. Forecasting of plume dispersion

Figures 4 and 5 present the 2-D nowcasting tephra concentration results of plume dispersion. Figures C.4-C.5 in **Appendix C** present the ensemble members of nowcasting scenarios of M05 and M06, respectively.

Preprints (www.preprints.org) | NOT PEER-REVIEWED | Posted: 23 November 2021 doi:10.20944/preprints202111.0422.v1

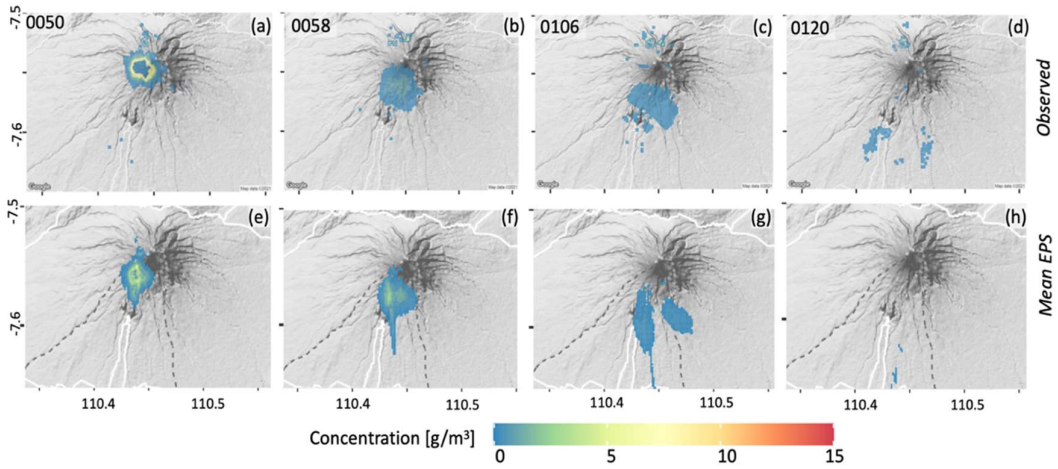

Figure 4. The retrieved tephra concentration on M05 from observed radar (a-d) compared to the mean-EPS (e-d) at different time steps, as indicated on top-left corner. The mean-EPS uses a threshold of tephra concentration ≥ 0.01 g/m³. In each image, *x*-axis is longitude and *y*-axis is latitude.

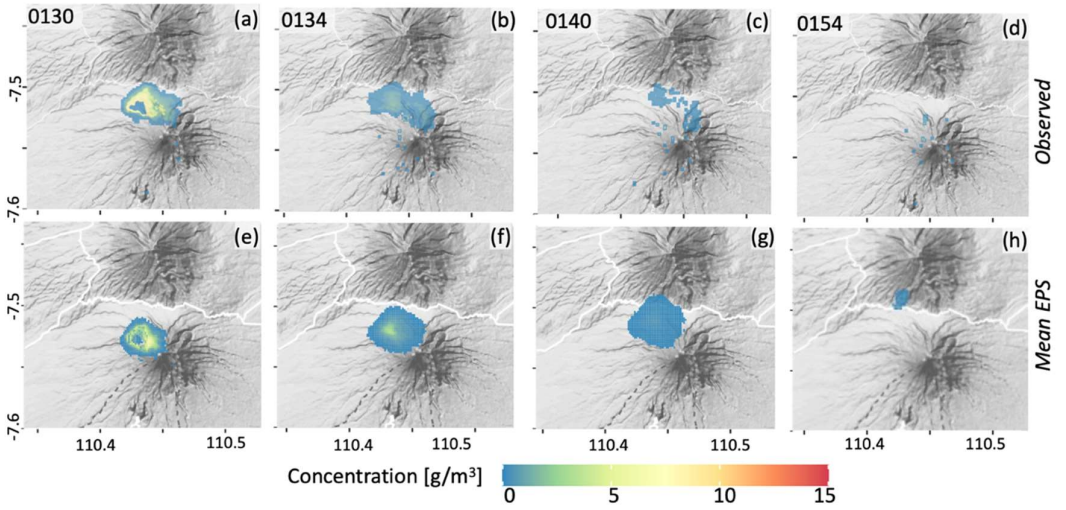

Figure 5. The retrieved tephra concentration on M06 from observed radar (a-d) compared to the mean-EPS (e-d) at different time step, as indicated on top-left corner. The mean-EPS uses a threshold of tephra concentration ≥ 0.01 g/m³. In each image, *x*-axis is longitude and *y*-axis is latitude.

3.3. Evaluation

The predictability scores are presented by *CSI*, *POD*, and *BS*. Both *CSI* and *POD* are given in Figure 6, while *BS* is shown in Figure 7. In the case of *BS*, we also calculated the score by comparing the ensemble members with Himawari-8 data. The area of volcanic ash identified by Himawari-8 overlying the mean EPS results is presented in Figure 8. Predictability indices generally agree that the highest uncertainty was given by the pair of onset+8-min and Sc5 members. The value of BS decreased through time but then increased, indicating the failure estimation of correct growth and decaying rate of some members.

Preprints (www.preprints.org) | NOT PEER-REVIEWED | Posted: 23 November 2021 doi:10.20944/preprints202111.0422.v1

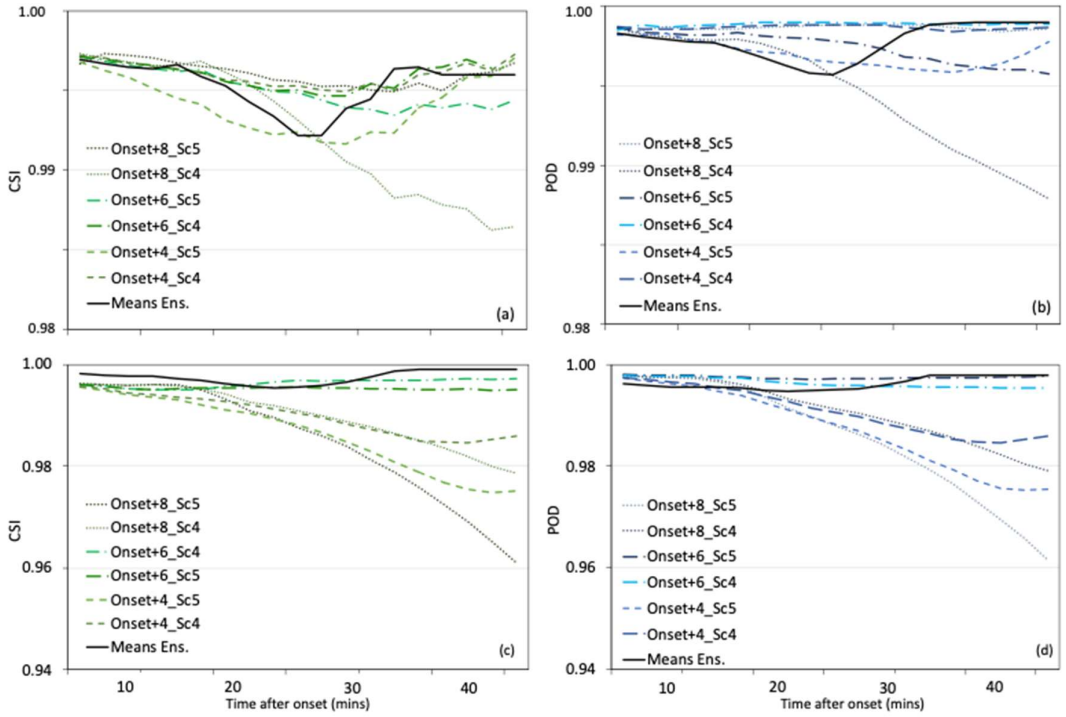

Figure 6. Spaghetti plots of *CSI* (left) and *POD* (right) for both study cases. (a) and (b) are for M05, while (c) and (d) are for M06. The ensemble member was named based on IC: onset+*i*_Sc*j*, where *i* and *j* represent the time in minutes and advection phenomena (Table 2), respectively.

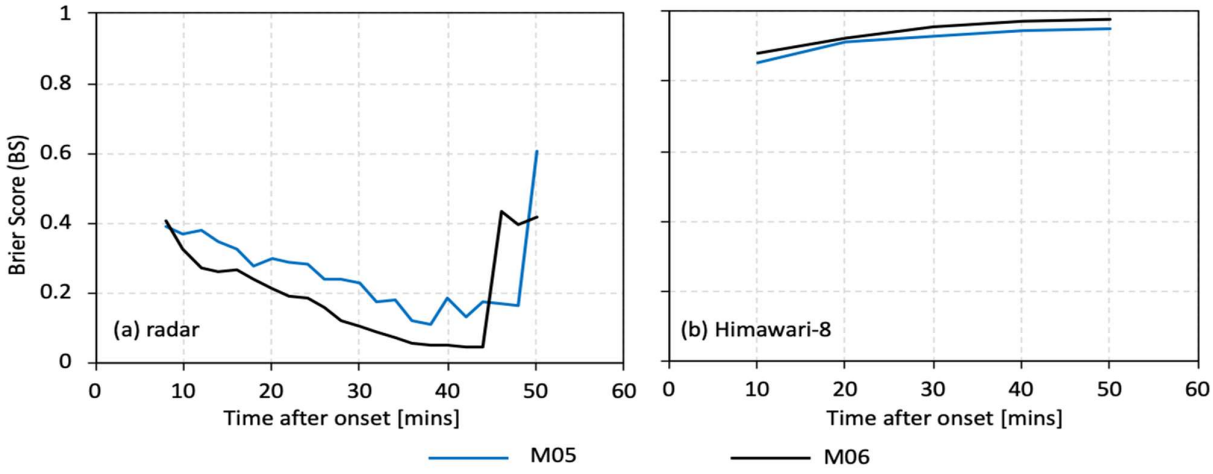

Figure 7. Brier score of tephra plume tracking by EPS of M05 and M06 based on the pair analysis with (a) radar and (b) Himawari-8. Each of EPS were generated using six members.

Preprints (www.preprints.org) | NOT PEER-REVIEWED | Posted: 23 November 2021 doi:10.20944/preprints202111.0422.v1

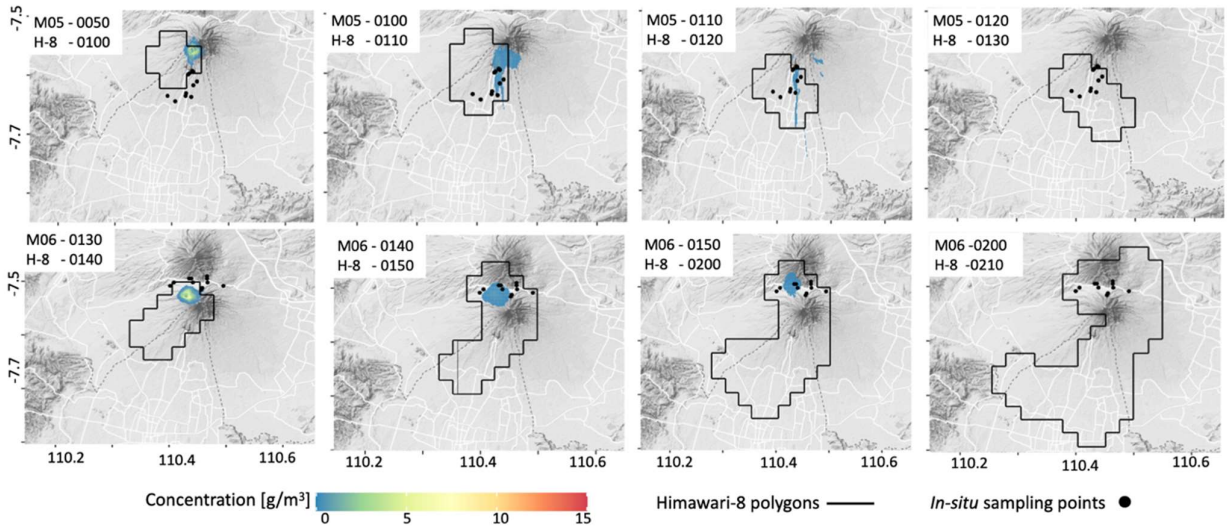

Figure 8. Mean ensemble of tephra concentration and area of detected tephra cloud by Himawari-8 (given by black polygons). The study cases and time stamps are indicated at top-left corner. The detected area of Himawari-8's tephra cloud was transformed into polygon using cloud temperature < 285 K. The ground-based data points are also presented in each map, given by black dots. In each image, x-and y-axis are longitude and latitude, respectively.

4. Discussion and Conclusions

4.1. Tephra Detection

Applying unwanted clutter cancellation is an important step in radar data processing. Here, we presented a simple procedure that could be easily included in the radar processing routine. In Table A.3, elevation angle 18° had the highest probability of misclassification (p = 0.3), while other elevation angles performed relatively better ($p \leq 0.1$). The misclassification can reduce numbers of Z_Hs associated with tephra. As presented in Figure A.1, a significant number of Z_H pixels in the SW and NW sectors of M06 were removed at elevation angles 15°and 18° after applying the NBC. Aggregating the Z_H (max) from elevation angles 13-21° helped restore most of the data in the NW but was still unable to reserve the echoes in the SE sector (Figure 2). This limitation is the consequence of a higher frequency of clutter in the SE sector. When the radar was pointing to Merapi vent, the sidelobes have contact with the hill side of Merapi (Turgo Hill, Figure 1), producing unwanted radar noises in this sector.

The radar-retrieved tephra had particle diameters ranging from 0.02 to 2.3 mm or ϕ 1.7 to -0.37 (Figures C.2 and C.3), indicating the limitation of the used X-MP radar in detecting larger and finer particle regimes. Particles larger than 2 mm (lapilli regime) were retrieved from Z_H until up to 4-mins after the onset, as they formed part of the eruptive mixture in the early development stages [39]. The limitation in radar-retrieved GSD is related to radar specification (e.g., antenna gained, wavelength, radar sensitivity, scanning speed). Larger tephra particles fall faster, and such speed might be unmonitored by the 2-mins temporal resolution of scanning radar. Moreover, based on the microphysical model of radar used in the tephra retrieved model, higher tephra concentrations can also be associated with greater amounts of finer tephra slower-falling particles within a sampling volume.

As noted earlier, we failed to extract radar estimates of GSD for M05 at two radar sampling points with available information of *in-situ* data (P-01, P-09, Figure 3). We could only extract the radar retrieved GSD at some points near P-01. While this study confirmed the incomparability between atmospheric and surface level data, we could use ground-based tephra grain size data to constrain and compare the range of grain sizes inferred from radar. Point Q-01 and Q-09 are close and distal to the vent, respectively, and thus

Preprints (www.preprints.org) | NOT PEER-REVIEWED | Posted: 23 November 2021 doi:10.20944/preprints202111.0422.v1

reflect the end members of the GSD for the whole sample region. However, based on conclusion in [23], there was no significant difference between the sortation in both points, where they categorized the GSD to be moderately well sorted. On the other hand, the extracted radar retrieved GSD have limited distribution ranging from $\phi = 0–1.25$. This limitation is related to the Rayleigh scattering theorem used in this study, which limits the 3.3 cm wavelength of radar to be associated with ~2 mm mean particle diameter.

While the estimated GSD from radar retrieved model was slightly greater than the *in-situ* data (for M06), the majority of retrieved radar GSD fell within the range observed in [23] (Figure 3). More importantly, the radar retrieved model could capture the spatial change in GSD, where the number of coarser particles decrease at a distant point from radar (Q-09, Figure 3b). Radar-retrieved estimates of particle size also agreed with the conclusion of [23], that the tephra from M05 had coarser grain size than M06 (Figure 3b). The difference between GSD for the two case study events can be attributed to the level of the eruption's explosivity and surface energy consumption. An eruption with lower explosion energy (M05) produced coarser grain pyroclastic deposits than the higher explosion energy (M06) [40, 41]. However, it should be noted that the prediction of GSD by radar/from explosion energy is still an active area of research, and the variety of fragmentation processes and magma properties makes it difficult to construct a general relation between GSD and energy balance [41].

4.1. Forecasting the dispersal of tephra

Spatially, the mean EPS could track elevated tephra concentrations estimated by observed and valid Z_H. The initial conditions used have a significant role in the estimated tephra dispersal, where the longest and shortest time windows tend to have poorer predictive skills. The shortest time window (onset+4) members show the tendency of the tephra cloud to elongate in the y-direction (N-S), as it could not estimate the correct horizontal u-wind component (parallel to the x-axis: E-W), as presented in Figures C.5–C.6. This signature is more visible in M05 than M06, where the forecasted plume elongated in the NS direction (Figures 4 and 8). The plume expansion in the NS direction could also be attributed to the vertical growth or decaying rate as it showed the change of altitude along with the range distance. As the radar is located in the SW sector, the altitude of the radar scan increases with radar's range in the N sector. The aggregated maximum Z_H from different elevation angles (13-21°) may represent the actual growing or decaying rate at a different height. The ejected material with a higher concentration would have reached a higher altitude before expanding horizontally within a shorter period (onset+4). This result explained the more intense concentration estimates in the NW sector for both cases. Hence, the translation model might have calculated an increasing trend of Z_H along the y-direction (NS), resulting in the NS elongated orientation of plume expansion. On the other hand, the most extended time window (onset+8) members showed an expansion of the plume to the u-wind component, indicating underestimation of growth and decaying rate (Figures C.5-C.6). At this time window, the identified plume had lost most of the intense Z_H (> 45 dBZ), causing an exaggeration of horizontal expansion.

Additionally, unlike precipitation, the advection vectors that determine the rotation and translation of tephra displacement were generated from fewer sample points, resulting in a higher error rate. Despite these limitations, this method has confirmed the time-dependent plume evolution exhibited in short-lived Vulcanian eruptions [42]. We can also recommend using onset+6 as the initial condition on time-lagged nowcasting of short-lived volcanic plume. This study presents that onset+6 can be the proper initial time to run the nowcasting model following an explosive event. It can cover both the plume expansion (related to the energy release and ESP) and wind components. In the future, applying this method to larger magnitude eruptions will be valuable to determine the optimum lead time for nowcasting application in the volcanic ash dispersal. A plume generated from a larger scale and longer duration eruption event may last longer in the atmosphere and cover a broader area in radar's azimuth display. A longer time window, which

 doi:10.20944/preprints202111.0422.v1

is not so soon after the start of the eruption (up to 6-hr), was recommended in the satellite-based ensemble prediction of volcanic ash dispersal from the VEI-4 Kelud eruption [13]. This longer time window is not applicable for our study cases, as they are short-lived plumes.

In general, both *CSI* and *POD* show a typical behaviour of nowcasting, where it decreases following the time increase. The mean EPS can reduce the uncertainty of forecasted tephra track, spatially and temporally (Figures 4-7). As presented in Figures 7 and C.6, some ensemble members of M05 and M06 show poorer skill with increased time. However, the *CSI* and *POD* of the mean EPSs are always maintained at greater than 0.99. In general, M05 has a better predictability rate than M06. The shorter duration but greater magnitude of M06 has a higher rate of tephra dispersion, indicated by its short-lived visibility on radar images. This result can be attributed to two reasons: first, M06 may produce higher growth and decaying rate that cannot be estimated correctly by the nowcasting model; second, the plume exceeds the radar's observable elevation angles. Combining the model's parallel translation, rotation, and growth and decaying rate produced the poorest forecasts as the dispersion of the small size plume is mainly related to wind-vectors and not by a mesoscale rotational motion, such as the case of a tropical cyclone. However, it should be noted that the higher predictability score given by *CSI* and *POD* is based on large numbers of zero-valued pixels. The observed radar range was fixed at 30 km (Table 1) with 150 m mesh resolution, resulting in significant N_{hit} generated from pairs of zero-valued pixels. Visual verification is crucial to conclude if each ensemble member can correctly imitate the tephra plume's movement and expansion.

Brier score (*BS*) provides more reliable results for predictability rate as it only counts pairs of occurrence and non-occurrence events (Eq. 5). The cross-validation of the observed radar involving all ensemble members increases the predictability rate until 40-mins after the onset, with BS ranging at 0.4 to 0.2. After 40-mins, the model performance becomes significantly poorer because of the accumulated error of incorrect growth decaying rate given by some ensemble members. Although all the predictability rate parameters indicate the tendency of skill to decrease with time, we still highlight the importance of EPS in improving the accuracy of the tephra forecast.

Comparing the temporal and spatial of mean EPS to Himawari-8 data (Figures 7b-8) gives the impression that the use of weather radar is limited in detecting the finest regime of the plume. In Figure 7b, the cross-validation of the ensemble members with cloud temperature (Himawari-8) gives *BS* ranging from 0.85 to 0.90 within the first 20-mins after the onset. The *BS* became poorer after 30-mins (> 0.95). Such poor *BS* is understandable due to the different spatial patterns of the ash cloud seen by the two sensors because of the attenuation of different particle size sensitivity [31]. Himawari-8 infrared observation (λ = 10.4 μm for BTD_{13}) is more sensitive to capture finer particle than the X-band radar observation (λ = 3.3 cm). The difference is more noticeable for M06, as the undetected tephra plume of Himawari-8 by the EPS model occurred in the S sector, which has the lowest elevation scanned by radar. Hence, the nowcasting could not capture the advection vectors and growth and decaying rate in this area (S sector).

Generally, finer particles are easily transported to higher elevations and dispersed farther away from the volcano. Hence, the detected tephra observed by radar was more likely to fall close to the volcano. This assumption is supported by the spatial distribution of forecasted radar-retrieved concentrations to have better agreement with *in-situ* sampling points than the Himawari-8 images (Figure C.3). Hence, this study reveals the benefit of the X-band radar for a local early warning system in tephra hazard management, which is essential for the nearby population. Even though the comparison between Himawari-8 and estimated radar tephra concentration is not directly comparable due to different resolution, sensor's wavelength, and parameters observed, the comparison is still important. It helps differentiate parts of the plume that will fall earlier (ground-based radar) and parts of the finer ash regimes within a plume that may be transported at higher altitude and potentially cause disruption to aviation (satellite). Moreover, the estimated

tephra concentration from the radar is essential information for the characteristic of the plume in the lower altitude, which cannot be retrieved from the satellite data [17].

While more work is needed to apply the remote sensing approach of tephra tracking using ground-based weather radar, this study has presented the potential use of weather radar to forecast the dispersal of tephra. In order to overcome the limitation of observing only part of the volcanic plume with ground-based weather radar [18,19], future work will extrapolate the estimated tephra concentration from a radio-wave sensor of radar into IR satellite data. Such a study will solve the classical problem of not detecting fine ash by radar observation while simultaneously improving the efficiency of the volcanic plume estimation by satellite data. This multisensory approach may allow tephra properties to be retrieved from satellites without acquiring ESP information. It can reduce the complexity of tephra plume dispersion modelling and improve the reliability of its real-time forecasting using remote sensing techniques.

Supplementary Materials: Tephra radar retrieved algorithms and its 2-D visualization are coded in RStudio scripts and published on GitHub (https://github.com/irasyarif1906/TephraRadar.git).

Author Contributions: Conceptualization, M.S., R.I.H., S.J., and B.T.; methodology, M.S., R.I.H.; software, M.S., R.I.H.; validation, M.S., R.I.H., and Q.Y.; formal analysis, M.S.; investigation, M.S.; resources, M.S., S.J., B.T.; data curation, N.A., D.L., H.G.M.; writing—original draft preparation, M.S.; writing—review and editing, M.S., S.J., B.T., Q.Y., R.I.H., and A.B.A.; visualization, M.S.; supervision, S.J.; project administration, N.A.; funding acquisition, S.J., M.S. All authors have read and agreed to the published version of the manuscript.

Funding: This research was supported by the Earth Observatory of Singapore via its funding from the National Research Foundation Singapore and the Singapore Ministry of Education under the Research Centres of Excellence initiative. This work comprises EOS contribution number 420.

Data Availability Statement: Radar data used in this study and tephra tracking module (radar nowcasting) are available upon request.

Acknowledgments: We thank The Japan Science and Technology Agency for facilitating the installation of X-MP radar through Grant-in-Aid for Science and Technology Research Partnership for Sustainable Development Program (SATREPS). We are indebted to CVGHM and laboratory of Hydraulic, Department of Civil Engineering and Environment, Gadjah Mada University, which have supported us with the raw data of the X-MP radar. Himawari-8 gridded data are distributed by the P-Tree of the Japan Aerospace Exploration Agency (JAXA) Earth Observation Research Centre (EORC) and JMA.

Conflicts of Interest: "The authors declare no conflict of interest.".

Appendix A Naïve Bayesian Classifier

A general expression of Bayes classifier is given in eq. (A.1). The classification is performed by applying the Bayes rule to calculate the probability of class c, given a particular set of input measurements, and the prediction is

$$p(c_\alpha|x_1,\dots,x_\beta) = \frac{p(x_1,\dots,x_\beta|c_\alpha)p(c_\alpha)}{p(x_1,\dots,x_\beta)} \quad (A.1)$$

In eq. (A.1) $p(c_\alpha|x_1,\dots,x_\beta)$ is the joint probability model, which can be simplified by assuming that all the input measurements are conditionally independent given the class label c. Subscript β denotes number of parameters, which are 5 and 1 for clutter and tephra class classification respectively. $p(c_\alpha)$ is the probability of the class label and subscript α have 3 and 6 classes for clutter cancelation and tephra detection, respectively.

Five input measurements for clutter classification were presented in Table A.1. They are reflectivity intensity Z_H and its standard deviation $\sigma(Z_H)$, altitude z, copolar correlation ρ_{HV}, and Frequency clutter map Pc. Pc was calculated by analysing a sufficient number of scans during a clear sunny day, which in this study was 210 sets data for each nine elevation angles. These data were obtained from 1 July 2018 (0700-1200 UTC) and 31 May 2018 (2200-2400 UTC). Every pixel in each scan had a probability of occurrence of being

Preprints (www.preprints.org) | NOT PEER-REVIEWED | Posted: 23 November 2021 doi:10.20944/preprints202111.0422.v1

clutter in the range of 0-1. For instance, if a particular pixel was detected as an echo in clear conditions without prior information of rainfall or eruptive events 100 times out of 200, then the pixel has a Pc = 0.5. Pc was calculated in a similar way for every elevation angle.

Table A.1 Input measurements of clutter classification

Z_H	$\sigma(Z_H)$	z
ρ_{HV}	Pc	

Training and test data for clutter classification were taken randomly from radar scanning data on 26-30 January 2018. Here, we assumed valid rainfall echo is similar to tephra. Figure A.1 presents an example of clutter cancellation results for elevation angles 15° and 18°.

The tephra classification relied on a single input measurement of Z_H. The classification of tephra used six sets of synthetic data to train and test the Bayesian classifier. The synthetic data were generated using Gaussian distribution and the statistical parametrization presented in Table A.2. Two of the parameters were considered in generating the synthetic data: particle size and concentration. The synthetic data were generated with the assumption that the standard deviation was proportional to 20 % and 50% from the mean values of particle diameter and concentration, respectively. Table contingency errors for clutter and tephra classification are given in Table A.3 and A.4, respectively. The total probability along a column is always equal to one, whereas the input classes are listed in the columns. These tables are coloured to identify the probability of correct classification easily. In the tables, red represents probability of ≥ 0.90, blue represents values of 0.70 to < 0.90, green is 0.10 to <0.70, and yellow ≤ 0.10.

Table A.2. Statistical properties of synthetic tephra (modified from [9])

Concentration (g/m³)		**Diameter of particle classes (mm)**			
		Fine class (F)		**Coarse Class (C)**	
		Mean	Range	Mean	Range
		0.10	0.015-0.35	1.00	0.35- 6
Light (L)	Mean	0.10		0.10	
	Range	0.01-0.50		0.01-0.50	
Moderate (M)	Mean	1.00		1.00	
	Range	0.50-2.00		0.50-2.00	
Intense (I)	Mean	5.00		5.00	
	Range	2.00-10.00		2.00-10.00	

Preprints (www.preprints.org) | NOT PEER-REVIEWED | Posted: 23 November 2021 doi:10.20944/preprints202111.0422.v1

Table A.3. Contingency table of clutter classification by NBC

Class		Clutter	Non-Clutter	Invalid
Elevation angle 3°	Clutter	0.90	0.06	0.00
	Non-Clutter	0.10	0.94	0.00
	Invalid	0.00	0.00	1.00
Elevation angle 5°	Clutter	0.96	0.04	0.00
	Non-Clutter	0.04	0.96	0.00
	Invalid	0.00	0.00	1.00
Elevation angle 7°	Clutter	0.98	0.04	0.00
	Non-Clutter	0.02	0.96	0.00
	Invalid	0.00	0.00	1.00
Elevation angle 9°	Clutter	0.98	0.03	0.00
	Non-Clutter	0.02	0.97	0.00
	Invalid	0.00	0.00	1.00
Elevation angle 11°	Clutter	0.99	0.03	0.00
	Non-Clutter	0.01	0.97	0.00
	Invalid	0.00	0.00	1.00
Elevation angle 13°	Clutter	1.00	0.03	0.00
	Non-Clutter	0.00	0.97	0.00
	Invalid	0.00	0.00	1.00
Elevation angle 15°	Clutter	0.95	0.02	0.00
	Non-Clutter	0.05	0.98	0.00
	Invalid	0.00	0.00	1.00
Elevation angle 18°	Clutter	0.99	0.30	0.00
	Non-Clutter	0.01	0.70	0.00
	Invalid	0.00	0.00	1.00
Elevation angle 21°	Clutter	1.00	0.10	0.00
	Non-Clutter	0.00	0.90	0.00
	Invalid	0.00	0.00	1.00

Table A.4. Contingency table of tephra classification by NBC

Class		F			C		
		L	**M**	**I**	**L**	**M**	**I**
F (Fine class)	**L**	0.94	0.19	0.04	0.02	0.00	0.00
	M	0.06	0.78	0.18	0.05	0.01	0.00
	I	0.00	0.04	0.76	0.14	0.02	0.01
C (Coarse class)	**L**	0.00	0.00	0.02	0.71	0.22	0.07
	M	0.00	0.00	0.00	0.08	0.72	0.21
	I	0.00	0.00	0.00	0.00	0.04	0.72

Preprints (www.preprints.org) | NOT PEER-REVIEWED | Posted: 23 November 2021 doi:10.20944/preprints202111.0422.v1

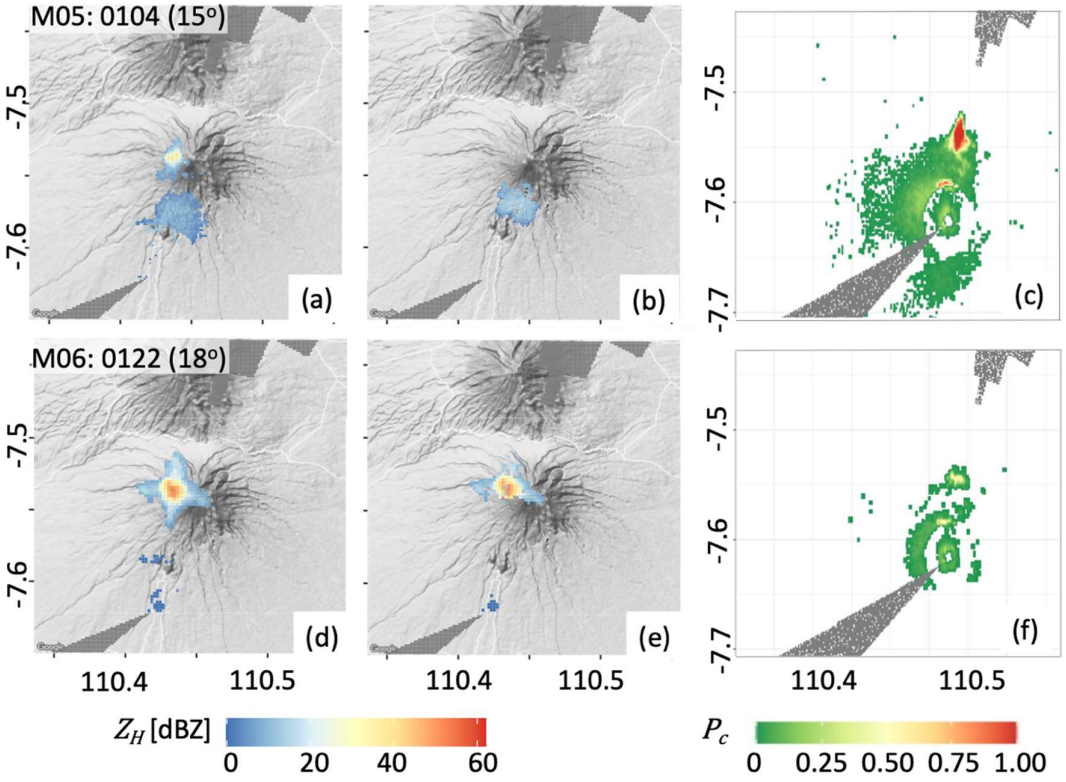

Figure A.1. An example of clutter cancellation results. Presented are for elevation angle 15 and 18°. The cases and time stamps are given in the top left corner. (a) and (d) are the observed radar reflectivity intensity Z_H, (b) and (e) are the filtered Z_H after applying the clutter cancellation procedure, and (c) and (f) are the frequency clutter map P_C for the given elevation angles. In each image, x-axis is longitude and y-axis is latitude.

Appendix B Microphysical radar model of tephra retrieval

The GSD of tephra is indicated by $N_a(D)$, where D [mm] is the particle diameter. The gamma GSD as a general scaled form of $N_a(D)$) [m^{-3}/mm] is formally expressed as

$$N_a(D) = N_n \left(\frac{D}{D_n}\right)^{\mu} e^{-\Lambda_n\left(\frac{D}{D_n}\right)^{\upsilon}} \tag{B.1}$$

Where D_n [mm] is the number-weighted mean diameter, N_n [m^{-3}/mm] is the intercept; Λ_n is the slope; μ is the shape factor; υ is the slope factor. The normalization is such that N_n and Λ_n are related to the mean diameter D_n and tephra concentration C_a, and have physical dimensions independent of μ and υ. The GSD form follows the scaled gamma distribution, which is derived from the analogue form established for raindrops. The scaled gamma GSD N_{SG} assumes that $\upsilon = 1$, and follows an equation similar to eq. (B.1):

$$N_{SG}(D;\mu,D_n,C_a) = N_{nG}\left(\frac{D}{D_n}\right)^{\mu} e^{-\Lambda_{nG}\left(\frac{D}{D_n}\right)} \tag{B.2}$$

where the intercept parameter N_{nG} and the slope parameter Λ_{nG} were scaled using eq. (B.3) and the tephra mass concentration was expressed in eq. (B.4)

$$\begin{cases} N_{nG} = C_a \dfrac{6{D_n}^{\mu}}{\pi\rho_a(3+\mu)!}\left[\dfrac{(\mu+1)!}{D_n(\mu!)}\right]^{3+\mu+1} \\ \Lambda_{nG} = \mu + 1 \end{cases} \tag{B.3}$$

Preprints (www.preprints.org) | NOT PEER-REVIEWED | Posted: 23 November 2021 doi:10.20944/preprints202111.0422.v1

$$C_a = \frac{\pi}{6}\rho_a m_3 \tag{B.4}$$

The n-th moment of gamma distribution is given by

$$m_n = \int_{D_1}^{D_2} D^n N_a(D) dD \tag{B.5}$$

Assuming $\mu = 1$, then an explicit expression of the complete moment of gamma distribution (i.e., when D_1=0 and D_2 =∞) can be written as follows

$$m_{nG} = \frac{N_{nG}}{(\Lambda_{nG})^{n+2}} D_n^{n+2-\mu} \Gamma(n+2) \tag{B.8}$$

Here Γ is the gamma function. N_{nG} and Λ_{nG} are derived from equation (B.3). In the Rayleigh scattering assumption, the radar reflectivity intensity Z_H is given by the sixth moment of gamma distribution in equation (B.9). Z_H can be expressed in mm/m^6 or dBZ, which is 10log$_{10}$ (Z_H[mm/m^6]).

$$Z_H = \int_{D_{min}}^{D_{max}} D^6 N_a(D) dD = m_6 \tag{B.9}$$

The generated synthetic Z_H was fitted against synthetic C_a to formulate a statistical parametric model of C_a-Z_H as follow

$$\hat{C}_a^{(c)} = \gamma [Z_H]^{\delta} \tag{B.10}$$

where γ and δ are the constants and the law-exponents. The apex (^) indicates estimated quantity, and superscript (c) indicates six classes of tephra (Table A.2).

Appendix C Spatio-temporal forecasting of tephra evolution and cross validation

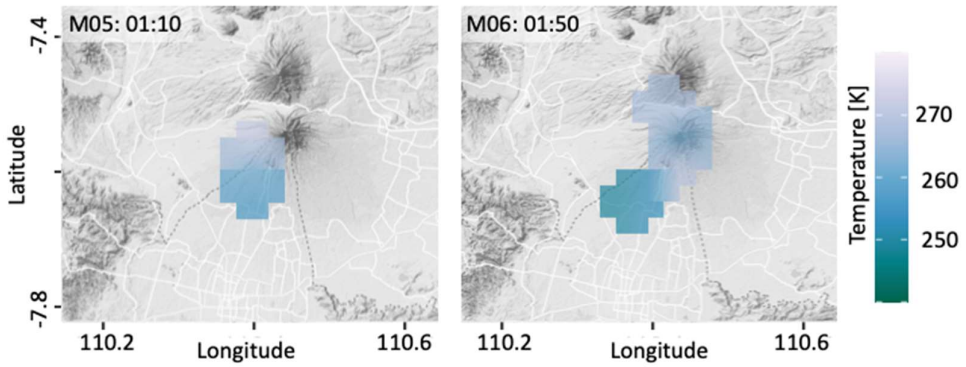

Figure C.1 The Bright temperature difference of band-13 (BTD$_{13}$) of Himawari-8. Presented here is for M05 (left) and M06 (right), 30 minutes after reported eruption onset, as indicated on top left corner.

Preprints (www.preprints.org) | NOT PEER-REVIEWED | Posted: 23 November 2021 doi:10.20944/preprints202111.0422.v1

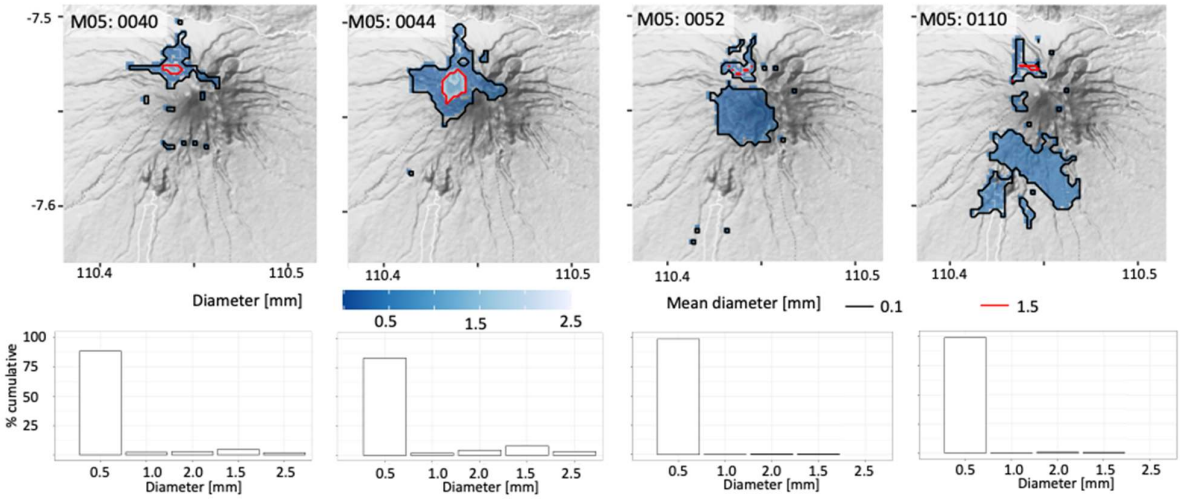

Figure C.2 First row is the spatial distribution of estimated radar retrieved mean diameter of M05 at different time stamps. Second row is the correspond cumulative grain size for each time stamp. In each image on the first row, x-axis is longitude and y-axis is latitude.

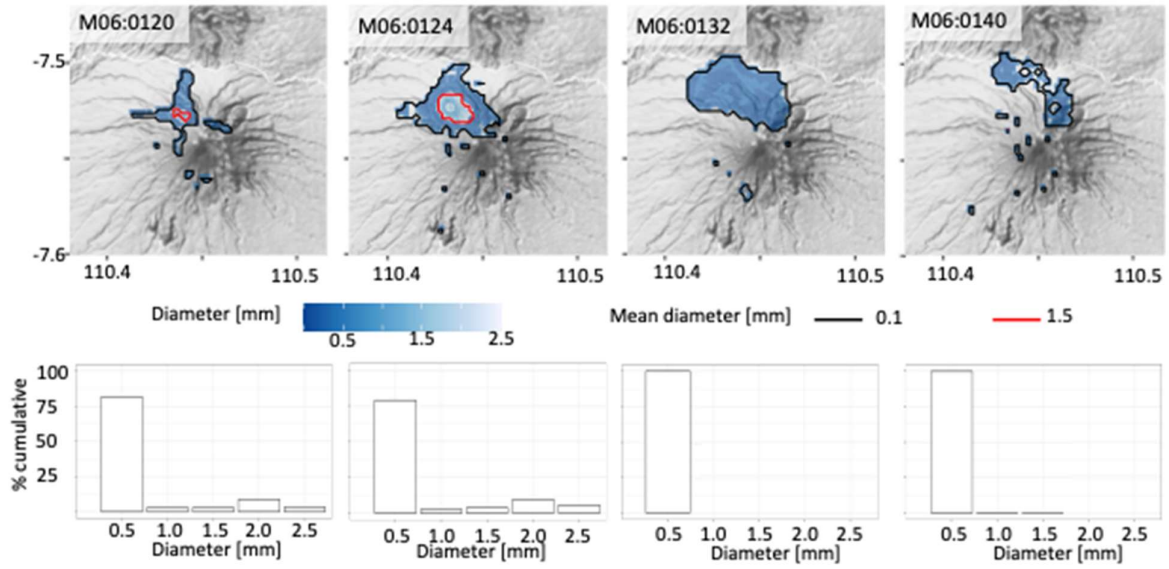

Figure C.3 First row is the spatial distribution of estimated radar retrieved mean diameter of M06 at several time stamps. Second row is the correspond cumulative grain size for each time stamp. In each image on the first row, x-axis is longitude and y-axis is latitude.

Preprints (www.preprints.org) | NOT PEER-REVIEWED | Posted: 23 November 2021 doi:10.20944/preprints202111.0422.v1

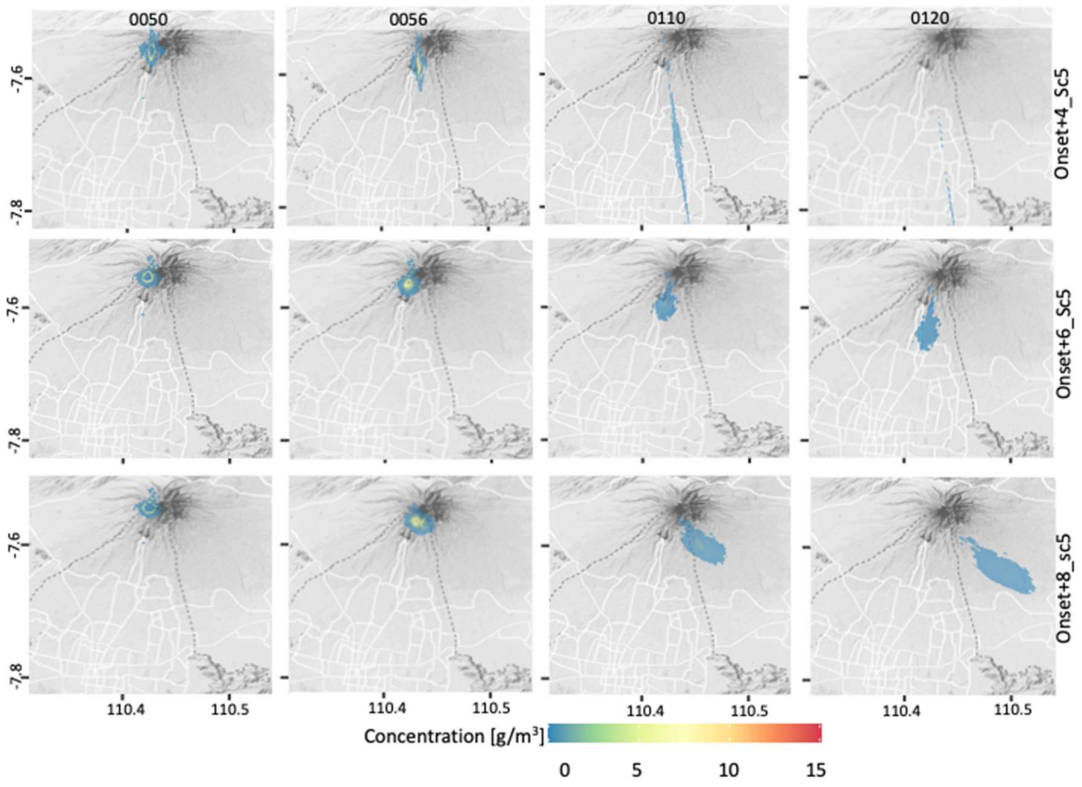

Figure C.4 Some examples of the ensemble members (row) at different time step output (column). Presented is the nowcasting of M05. Each of ensemble member was named based on initial condition: onset+*i*_Sc*j*, where *i* and *j* represent the time in minutes and advection scenario (Table 3), respectively. In each image, *x*-axis is longitude and *y*-axis is latitude.

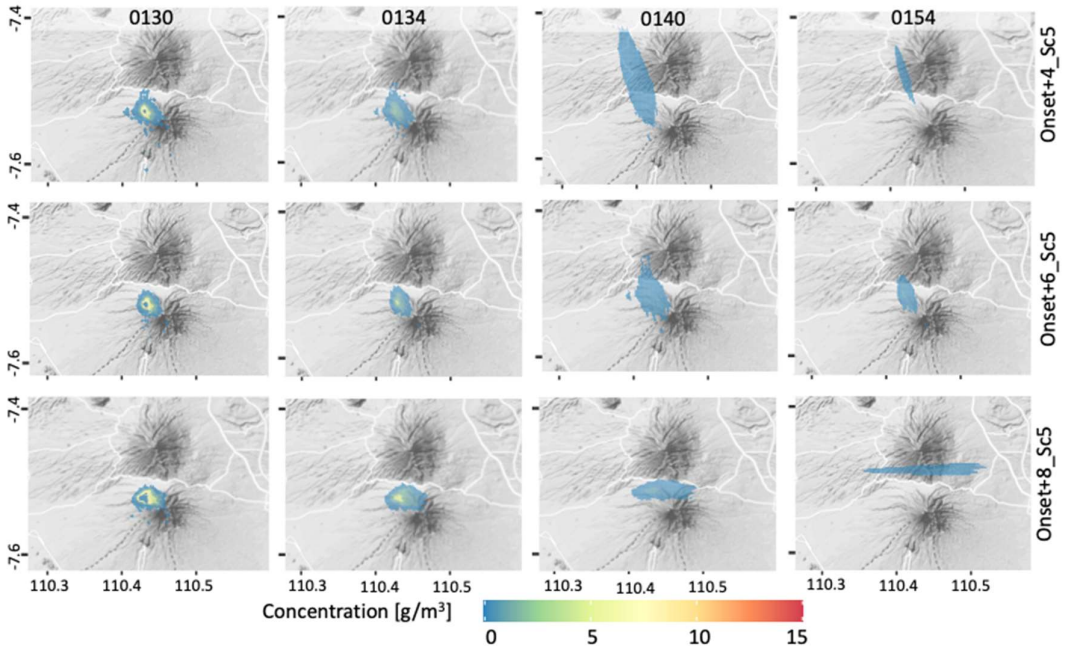

Figure C.5 Some examples of the ensemble members (row) at different time step output (column). Presented is the nowcasting of M06. Each of ensemble member was named based on initial condition: onset+*i*_Sc*j*, where *i* and *j* represent the time in minutes and advection scenario (Table 3), respectively. In each image, *x*-axis is longitude and *y*-axis is latitude.

Preprints (www.preprints.org) | NOT PEER-REVIEWED | Posted: 23 November 2021 doi:10.20944/preprints202111.0422.v1

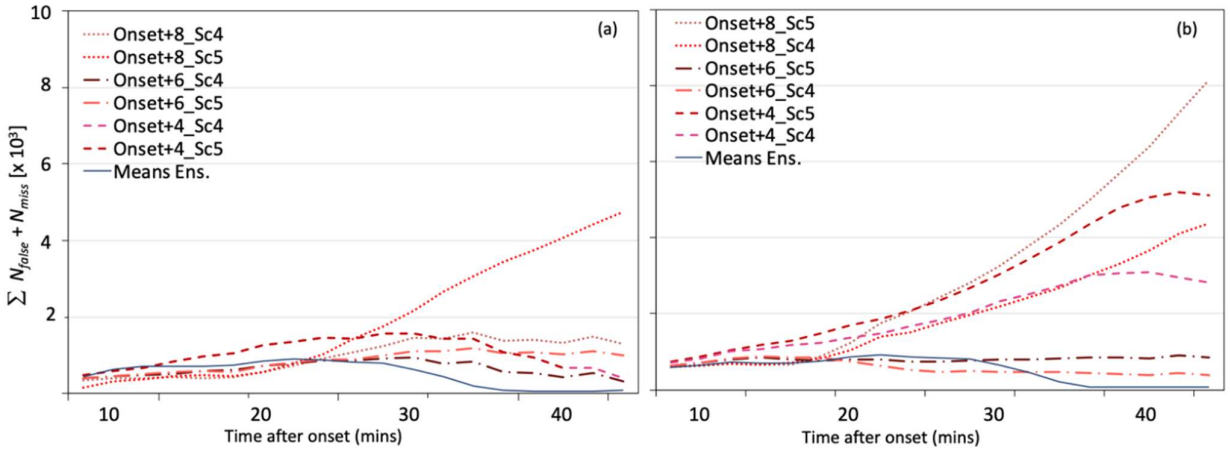

Figure C.6 Number of missed and false events of ensemble members and the mean ensemble for M05 (a) and M06 (b).

References

1. Williams, G.T.; Jenkins, S.F.; Biass, S.; Wibowo, H.E.; Harijoko, A. Remotely assessing tephra fall building damage and vulnerability: Kelud Volcano, Indonesia. *J Appl. Volcanol*. **2020**, 9, 10. https://doi.org/10.1186/s13617-020-00100-5.
2. Jenkins, S.F.; Wilson, T.M.; Magill, C.; Miller, V.; Stewart, C.; Blong, R.; Marzocchi, W.; Boulton, M.; Bonadonna, C.; Costa, A., in Volcanic ash fall hazard and risk. In *Global Volcanic Hazards and Risk*, Loughlin, S., Sparks, S., Brown, S., Jenkins, S., and Vye-Brown, C., Eds.; Cambridge University Press, Cambridge, 2015, pp. 359-370. https://doi.org/10.1017/CBO9781316276273.005.
3. Jenkins, S.F.; Spence R.J.S; Fonesca, J.F.B.D.; Solidum, R.U.; Wilson, T.M. Volcanic risk assessment: quantifying physical vulnerability in the built environment. *J Volcanol. Geotherm. Res*. **2014**, 276:105–120. https://doi.org/10.1016/j.jvolgeores.2014.03.002.
4. Donnadieu, F.; Freville, P.; Hervier, C., Coltelli, M.; Scollo, S.; Prestifilippo, M.; Valade, S.; Rivet, S.; Cacault, P. Near-source Doppler radar monitoring of tephra plumes at Etna. *J. Volcanol. Geotherm. Res*. **2016**. 312, pp. 26–39. http://dx.doi.org/10.1016/j.jvolgeores.2016.01.009.
5. Donnadieu, F. Volcanological Applications of Doppler Radars: A Review and Examples from a Transportable Pulse Radar in L-Band. In Doppler Radar Observations-Weather Radar, Wind Profiler, Ionospheric Radar, and Other Advanced Applications, Bech, J., Chau, J.L., Eds. InTech, 2012. http://dx.doi.org/10.5772/35940.
6. Marzano, F. S.; Picciotti, E.; Di Fabio, S.; Montopoli, M.; Mereu, L.; Degruyter W.; Bonadonna, C.; Ripepe, M., Near-Real-Time Detection of Tephra Eruption Onset and Mass Flow Rate Using Microwave Weather Radar and Infrasonic Arrays. *IEEE Trans. Geosci. Remote Sen*. **2016**, 54, 11, pp. 6292-6306. http://dx.doi.org/10.1109/TGRS.2016.2578282.
7. Oishi, S.; Iida, M.; Muranishi, M.; Ogawa, M.; Hapsari, R.I.; Iguchi, M. Mechanism of volcanic tephra falling detected by X-band multi parameter radar. *J. Disaster Res*. **2016**, 11, 1, pp. 43-45. https://doi.org/10.20965/jdr.2016.p0043.
8. Marzano, F.S.; Vulpiani, G.; Rose, W.I. Microphysical characterization of microwave radar reflectivity due to volcanic ash clouds. *IEEE Trans. Geosci. Remote Sen*. **2006**, 44, 2, 313-327.
9. Marzano, F.S; Vulpiani, G.; Barbieri, S.; and Rose, W.I. Volcanic ash cloud retrieval by ground-based microwave weather radar. IEEE Trans. Geosci. Remote Sen. **2006**, 44, 11, 3235-3246.
10. Montopoli, M.; Vulpiani, G.; Marzano, F.; Piccioti, E.; Di Fabio, S. Interpretation of polarimetric radar measurements at X-band for Volcanic plume monitoring. ERAD 2014 – The Eight European Conference on radar in Meteorology and Hydrology, Garmisch-Partenkirchen, Germany, 1-8 September 2014.
11. Marzano, F.S.; Picciotti, E.; Montopolli, M.; Vulpiani, G. Inside volcanic clouds – Remote sensing of ash plumes using microwave weather radars. *Bull. Am. Met. Soc*. **2013**, 94, 1567–1586.
12. Shiiba, M.; Takasao, T.; Nakakita, E. Investigation of short-term rainfall prediction method by a translation model, Jpn. Conf. on Hydraulic, 28th, 1984, pp.423-428.

13. Hapsari, R.I.; Oishi, S.; Sunada, K.; Sano,T. Improving flood simulation in urban river basin using X-band polarimetric radar and distributed hydrological model. *Ann. J. of Hydra. Eng.-JSCE, Ser. B1*. **2010**, 54, pp. 121-126.
14. Hapsari, R.I.; Oishi, S.; Sunada, K.; Nakakita, E.; Sano, T. Singular vector method on short-term rainfall prediction using radar for hydrologic ensemble prediction. *Ann. J. of Hydra. Eng.-JSCE, Ser. B1.* **2011**, 67, 4, pp. I_109-I_114. https://doi.org/10.2208/jscejhe.67.I_109.
15. Hapsari, R.I. Development of probabilistic hydro-meteorological prediction for urban flood disaster prevention. Ph.D. Thesis, University of Yamanashi, Japan, September 2011.
16. Hapsari, R.I.; Oishi, S.; Syarifuddin, M.; Asmara, R.A.; Legono, D. X-MP Radar for Developing a Lahar Rainfall Threshold for the Merapi Volcano Using a Bayesian Approach. *J. Disaster Res.* **2019**, 14, 5, pp. 811-828. https://doi.org/10.20965/jdr.2019.p0811.
17. Zidikheri, M.J.; Lucas, C.; Potts, R. J. Quantitative verification and calibration of volcanic ash ensemble forecasts using satellite data. *J Geophys. Res-Atmos*. **2018**, 123, pp. 4135–4156. https://doi.org/10.1002/2017JD027740.
18. Syarifuddin, M.; Oishi, S.; Hapsari, R.I; Shiokawa, J.; Mawandha, H.G.; and Iguchi, M. Estimating the Volcanic Ash Fall Rate from the Mount Sinabung Eruption on February 19, 2018 Using Weather Radar. *J. Disaster Res*. **2019**, 14, 1, pp. 135-150. https://doi.org/10.20965/jdr.2019.p0135.
19. Syarifuddin, M.; Oishi, S.; Nakamichi, H.; Maki, M.; Hapsari, R.I.; Mawandha, H.G.; Aisyah, N.; Basuki, A.; Loeqman, A.; Shimomura, M.; Iguchi, M. A real-time tephra fallout rate model by a small-compact X-band multi-parameter radar. *J Volcanol. Geotherm. Res*. **2020**, 405, 107040. https://doi.org/10.1016/j.jvolgeores.2020.107040.
20. Syarifuddin, M.; Oishi, S.; Hapsari, R.I.; Legono, D.; and Iguchi, M. Integrating X-MP Radar Data to Estimate Rainfall Induced Debris Flow in the Merapi Volcanic Area. *Adv. Water Resour*. **2017**, 110, 249-262. https://doi.org/10.1016/j.advwatres.2017.10.017.
21. Bringi, V. N., and V. Chandrasekar, Polarimetric Doppler Weather Radar: Principles and Applications. 2001, Cambridge University Press, Cambridge.
22. Furuno. Operator Manual: Compact X-band dual polarimetric weather Doppler radar, type WR-2100. 2014, Japan.
23. Setijadji, L.D., Jesslyn, J., Situmorang, N.G., Wiguna, A., 2018 eruption of Merapi: The interpretation of eruption type based on volcanic material study from explosive eruption on May 11 and June 1, 2018 (in Bahasa Indonesia). Proceeding Seminar Nasional Kebumian 11, Yogyakarta, Indonesia, 5-6 September 2018, pp. 908-917, Available online: https://repository.ugm.ac.id/274920/1/OVK-3_ERUPSI%20MERAPI%202018%20INTERPRETASI%20JENIS%20ERUPSI%20BERDASARKAN%20STUDI%20MATERIAL%20VULKANIK%20HASIL%20ERUPSI%20EKSPLOSIF%2011%20MEI%20DAN%201%20JUNI%20201.pdf (accessed on August 15, 2020).
24. Budi-Santoso, A.; Humaida, H.; Sulistiyani; Aisyah, N.; Putra, R.; et al. The 2018 phreatic eruption, an Indication of new magmatism episodes of Merapi. In Bahasa Indonesia: Letusan Freatik 2018 Indikasi Episode Baru Aktivitas Magmatis G. Merapi. Buletin Merapi, Edisi Agustus 2018. 2018, 22,02, pp 12-38.
25. Centre for Volcanology and Geological Hazard Mitigation (CVGHM). Press release of Mt. Merapi on June 6, 2018, at 10:00 (in Bahasa Indonesia). 2018, Available online: http://merapi.bgl.esdm.go.id/pub/page.php?idx=321 (accessed on 28 January 2019).
26. Rico-Ramirez, M.A.; Cluckie, I.D. Classification of ground clutter and anomalous propagation using dual-polarization weather radar. *IEEE Trans. Geosci. Remote Sens*. **2008**, 46, pp. 1892–1904. https://doi.org/10.1109/TGRS.2008.916979.
27. Lacasse, C.; Karlsdóttir, S.; Larsen, G.; Soosalu, H.; Rose, W.I.; Ernst, G.G.J. Weather radar observations of the Hekla 2000 eruption cloud, Iceland. Bull Volcanol. **2004**, 66, 457–473, https://doi.org/10.1007/s00445-003-0329-3.
28. Maki, M.; Iguchi, M.; Maesaka, T.; Miwa, T.; Tanaka, T.; Kozono, T.; Momotani, T.; Yamaji, A.; Kakimoto, I. Preliminary Results of Weather Radar Observations of Sakurajima Volcanic Smoke., J. Disaster Res. 2016, 11(1), 15-30.
29. Maki, M.; Kim, Y.; Kobori, T.; Hirano, K.; Lee, D.-I.; Iguchi, M. Analyses of three-dimensional weather radar data from volcanic eruption clouds. *J Volcanol. Geotherm. Res*. **2021**, 412, 107178, https://doi.org/10.1016/j.jvolgeores.2021.107178.
30. Marzano, F.S.; Barbieri, S.; Piccioti E.; Karlsdottir. Monitoring sub-glacial volcanic eruptions using C-band radar imagery. *IEEE Trans. Geosci. Remote Sens.* **2009**, 48, 1, pp. 403-414. https://doi.org/10.1109/TGRS.2009.2024933.

31. Corradini, S.; Montopoli, M.; Guerrieri, L.; Ricci, M.; Scollo, S.; Merucci, L.; Marzano, F.S.; Pugnaghi, S.; Prestifilippo, M.; Ventress, L.J.; Grainger, R.G.; Carboni, E.; Vulpiani, G.; Coltelli, M. A Multi-Sensor Approach for Volcanic Ash Cloud Retrieval and Eruption Characterization: The 23 November 2013 Etna Lava Fountain. *Remote Sens*. **2016**, 8, 58. https://doi.org/10.3390/rs8010058.
32. Vinodkumar; Chandrasekar, A. Ensemble Lagged Forecasts of a Monsoon Depression over India Using a Mesoscale Model. *Atmosfera*. **2007**, 20, 1, pp. 25-44.
33. Bivand, R.; Keitt, T.; Rowlingson, B. rgdal: Bindings for the "Geospatial" data abstraction Library, R-Package version 1.5-18. 2020. https://CRAN.R-project.org/package=rgdal.
34. Kahle, D.; Wickham, H. ggmap: Spatial visualization with ggplot2. The R Journal, **2013**,1, pp. 144-161. http://journal.r-project.org/archive/2013-1/kahle-wickham.pdf.
35. Bessho, K.; Date, K.; Hayashi, M.; Ikeda, A.; Imai, T.; Inoue, H.; Kumagai, Y.; Miyakawa, T.; Murata, H.; Ohno, T.; Okuyama, A.; Oyama, R.; Sasaki, Y.; Shimazu, Y.; Shimoji, K.; Sumida, Y.; Suzuki, M.; Taniguchi, H.; Tsuchiyama, H.; Uesawa, D.; Yokota, H.; Yoshida, R. An introduction to Himawari-8/9 – Japan's new-generation geostationary meteorological satellites. J. *Meteor. Soc. Japan*, **2016**, 94, pp. 151-183. https://doi.org/10.2151/jmsj.2016-009.
36. Shimizu, A. Introduction to Himawari-8 RGB composite imagery. Meteorological satellite centre technical note, No.65, October 2020.
37. Roebber, P.J. Visualizing multiple measures of forecast quality. *Wea. Forecasting*. **2009**, 24, pp. 601-608. https://doi.org/10.1175/2008WAF2222159.1.
38. Wilks, D.S. Statistical methods in the atmosphere. Academic Press, 2011.
39. Tournigand, P.-Y.; Taddeucci, J.; Gaudin, D.; Peña Fernández, J.J.; Del Bello, E.; Scarlato, P.; Kueppers, U.; Sesterhenn, J.; Yokoo, A. The initial development of transient volcanic plumes as a function of source conditions. *J. Geophys. Res-Sol. Ea*. **2019**, 122, pp. 9784– 9803. https://doi.org/10.1002/2017JB014907.
40. Walker, G.P.L. Explosive Volcanic Eruptions – A New Classification Scheme, *Geol. Rundsch.* **1973**, 62, pp 431-446. https://doi.org/10.1007/BF01840108.
41. Gonnermann, H.M. Magma Fragmentation. *Annu. Rev. Earth and Pl. Sc.*, 2015, 43,1, pp 431-458. https://doi.org/10.1146/annurev-earth-060614-105206.
42. Scase, M.; Caulfield, C.; Dalsiel, S., Hunt. J. Time-dependent plumes and jets with decreasing source strengths. *J. Fluid Mech*. **2006**, 563, pp. 443-461. https://doi.org/10.1017/S0022112006001212.